CONSTRUCTION AND INITIAL OPERATION OF THE COLUMBIA NONNEUTRAL TORUS

T. SUNN PEDERSEN,* J. P. KREMER, R. G. LEFRANCOIS, and Q. MARKSTEINER
Columbia University, Department of Applied Physics and Applied Mathematics, New York, New York

N. POMPHREY, W. REIERSEN, and F. DAHLGREN
Princeton University, Plasma Physics Laboratory, Princeton, New Jersey

XABIER SARASOLA *Association Euratom-CIEMAT, Madrid, Spain*

Received November 28, 2005
Accepted for Publication March 30, 2006

We report on the results from initial testing and operation of the Columbia Nonneutral Torus, a new stellarator experiment constructed at Columbia University to study the confinement of nonneutral plasmas, electron-positron plasmas, and stellarator confinement in the presence of strong electrostatic fields. A new algorithm for automatic identification of good magnetic surfaces, island chains, and stochastic regions in Poincaré maps is also described. We present some of the details of the design of the interlocked in-vessel coils and the vacuum system and report on initial vacuum performance. Magnetic surface mapping and visualization results are also presented, confirming the existence of ultralow aspect ratio magnetic surfaces with excellent quality and good agreement with numerical calculations.

KEYWORDS: *stellarator, nonneutral plasma, magnetic confinement*

I. INTRODUCTION

The Columbia Nonneutral Torus (CNT) is a stellarator designed specifically to study the physics of nonneutral plasmas (partially neutralized as well as pure electron plasmas), electron-positron plasmas, and stellarator confinement in the presence of strong electric fields.[1–3] As described previously,[4] in order to access the relevant nonneutral plasma physics, and to construct the device quickly and inexpensively, the CNT stellarator design aimed to achieve the following:

1. good magnetic surface quality without large islands and ergodic regions, and resilience against magnetic field errors
2. ultrahigh vacuum level, $<3 \times 10^{-10}$ Torr, to prevent ion contamination and to make neutral interactions (such as neutral drag) negligible
3. a value of $\varepsilon\iota B$ large enough to allow the ratio of perpendicular to parallel dynamical time scales to be large. Here, ε is the inverse aspect ratio, ι is the rotational transform, and B is the magnetic field strength.
4. a simple coil system that could be constructed quickly and inexpensively
5. maximum physics flexibility, including the ability to change iota and shear profiles
6. a simple and inexpensive vacuum chamber, but one with good port access for vacuum pumps, diagnostics, etc.

Gourdon et al. investigated magnetic configurations[5] formed by circular, interlocked coils constructed on Villarceau circles. Starting from this simple coil configuration, studies were performed to optimize the tilt angle and aspect ratio of an interlocked pair of coils to best achieve the above-mentioned goals. The result of this optimization was a simple yet flexible and robust design. Four circular coils, one pair interlocked and placed inside the domed cylindrical vacuum chamber (the interlocked coils), and the other pair [the poloidal field (PF) coils] placed outside the vacuum chamber configured approximately as a Helmholtz pair, create ultralow aspect ratio magnetic surfaces with high tolerances to errors. The basic configuration is illustrated in Fig. 1.

Three distinct configurations can be achieved by varying the angle between the interlocked coils. The present configuration is characterized by being particularly

*E-mail: tsp22@columbia.edu

Fig. 1. The basic CNT configuration, showing the four coils and the resulting magnetic surface shaped inside the vacuum chamber.

error-field insensitive, with an ultralow aspect ratio ($A < 1.9$) and modest rotational transform and negative magnetic shear ($\iota = 0.12$ near the magnetic axis and $\iota = 0.22$ at the last closed flux surface). The other two configurations have larger (but still low) aspect ratios ($A = 2.3$ and $A = 2.7$), larger rotational transforms (up to 0.65), and little magnetic shear. The basic design is presented in a previous publication.[4]

In this article we report on some of the design and fabrication details, in particular for the ultrahigh vacuum (UHV)–compatible, reconfigurable in-vessel interlocked coils; a description of the vacuum bakeout and pumping system; and results from the actual vacuum performance in the CNT. We also describe a numerical tool capable of discerning good magnetic surfaces, island chains, and stochastic regions from a magnetic Poincaré plot. This tool, which is based on a simple, intuitive algorithm described here, may be useful for future stellarator optimization efforts. Results from the initial operation are presented, including initial vacuum performance, measurements of magnetic surfaces, and first pure electron plasma results.

II. AN ALGORITHM FOR DETECTING ISLANDS AND STOCHASTIC REGIONS IN A NUMERICALLY GENERATED POINCARÉ PLOT

A major concern in stellarator optimization is whether the configuration being studied or optimized has significant internal island chains or stochastic regions. Although rational surfaces and perhaps even associated internal island chains can be beneficial, for example, by creating transport barriers,[6] sizable island chains are generally not desired because the radial plasma density and temperature profiles are flattened in the vicinity of the island chains.[7] Stochastic regions provide even stronger flattening of profiles and rapid radial transport and are even less desirable. Computer optimizations of stellarators therefore should include some assessment of the magnetic surface quality, that is, an assessment of the fraction of the confined volume that is occupied by sizable island chains or stochastic regions. Approaches to this kind of characterization have been developed, generally requiring detailed a priori information about the magnetic configuration being studied, such as the rotational transform profile and the size of resonant magnetic harmonics at the rational surfaces.[8] On the other hand, a person can determine the good magnetic surfaces, island chains, and stochastic regions in a few seconds by visual inspection of a magnetic Poincaré map without any need for a direct mathematical analysis. A magnetic Poincaré map is the intersection of magnetic field lines with a cross-sectional plane, typically a φ = constant plane, where φ is a toroidal angle.

Here, we present a relatively simple set of computer algorithms to classify the points of a Poincaré map inspired by the way that humans distinguish good magnetic surfaces from island chains and stochastic regions when visually inspecting a numerically calculated Poincaré map. This method has some similarities with other geometrically based classification schemes for Hamiltonian maps, such as the KAM method[9] and a recent set of algorithms using machine learning and graph theory and applied directly to stellarator magnetic surfaces.[10] Our method relies on a few simple observations about the differences between how island chains, good magnetic surfaces, and stochastic regions manifest themselves as point distributions in a Poincaré map. As the number of points on a Poincaré map goes to infinity, the points associated with a good magnetic surface form an infinitely thin line that closes on itself (topologically, a distorted circle). A magnetic island chain manifests itself as a discrete number of clusters of points, each of which, by closer inspection and at a sufficient number of points per cluster, reveals itself as a distorted circle (the island). Between adjacent clusters there are gaps of a finite size. These gaps correspond to the regions around the x points of the island chain. It is the detection of the gaps that allows one to distinguish the island chains from good magnetic surfaces.

A stochastic region represents a continuous distribution of points, without gaps but with finite width and therefore area, as opposed to good magnetic surfaces, which are infinitely thin and do not cover a finite area in the Poincaré cross section. It is the detection of a finite width that allows one to distinguish a stochastic region from a good magnetic surface.

The detection algorithm uses as its input a Poincaré map calculated by following a particular magnetic field line through N toroidal transits. The map consists of the N points (x_i, y_i) on the Poincaré cross section where it intersects the magnetic field line. If the magnetic field line being followed lies on a good magnetic surface, these N points distribute themselves densely on the closed line $[x(s), y(s)]$ that defines the intersection of the magnetic surface with the Poincaré cross section. Here, s is a scalar that parameterizes the closed line. For magnetic surfaces that are not too concave, a convenient choice for s is the angle θ_i between the $y = 0$ line and the line going between a reference point internal to the magnetic surface and the Poincaré point of interest (x_i, y_i), $i = 1 \ldots N$. One can think of the θ_i as being the poloidal angles of the Poincaré points. The internal reference point [whose coordinates we denote by (X, Y)] can be chosen to be the magnetic axis or the center of mass of Poincaré points for the magnetic field line under investigation, $x_c = \Sigma\, x_i/N$, $y_c = \Sigma\, y_i/N$, although one should caution that the latter is not guaranteed to be internal to the magnetic surface presumably being mapped out. One should also caution that the angle θ does not always provide an adequate single-valued parameterization of the true magnetic surface curve if the magnetic surface is highly distorted away from a simple convex shape in the cross section being used for the Poincaré plot. However, in stellarators, one can often find some toroidal cross section where the Poincaré maps are convex enough for the above method to work for a suitably chosen internal point (X, Y). If this is not the case, then the present algorithm may not work. Once θ has been calculated for every Poincaré point i, $\theta_1 \ldots \theta_N$, the classification proceeds as follows: First, the θ_i values are sorted into a list θ_j in ascending order, $\theta_j < \theta_{j+1}$. The differences, or gaps, $\Delta_j = \theta_{j+1} - \theta_j$, $j = 1 \ldots N$, between neighboring θ values are computed, with the proper wraparound condition applied between 0 and 2π. The largest gap, i.e., the largest value of Δ_j, Δ_{max}, is determined. If Δ_{max} exceeds the threshold $2\pi g/N$, where g is a parameter that can be adjusted for optimum algorithm performance ($g = 80$ works well for the cases studied here), then a rational surface with an associated island chain is deemed to exist. If one can rule out $m = 1$ or $m = 2$ islands a priori (m is the poloidal mode number), an additional criterion is added: At least two other gaps of size greater than $\pi g/N$ must exist in addition to $\Delta_{max} > 2\pi g/N$. If these criteria are met, an island chain is presumed to be present; otherwise, the magnetic field line being followed either maps out an irrational (good) magnetic surface or a stochastic region. The extra criteria used for $m > 2$ island chains reduce the rate of false positives at any given value of g and thus allow for a smaller value of g, which gives higher sensitivity to high-order island chains.

If the Poincaré plot is deemed not to be an island chain, the radii of the Poincaré points $r_j = ((x_j - X)^2 + (y_j - Y)^2)^{1/2}$ are calculated to determine if the magnetic field line under investigation is mapping out a good magnetic surface or a stochastic (volume-filling) region. The variation in r_j should be very small compared with the average value r_j for any small interval $\theta_a < \theta_j < \theta_b$ if it is a good magnetic surface of zero thickness. Thus, by computing the fractional variation of r_j for groups of points binned by their values of θ, one can detect stochastic regions of a certain minimum size.

This rather simple method has been tested on Poincaré plots generated for two different systems: One is the so-called Standard Map, which exhibits the same topological features (stochastic regions, good surfaces, and island chains) as stellarator magnetic surfaces. The Standard Map is given by the following iteration formulas[11]:

$$x_{n+1} = x_n - k * \sin(2\pi\, y_n)/2\pi$$

and

$$y_{n+1} = y_n + x_{n+1} \ .$$

Here, k is a control parameter that can be used to change the topology of the map. Figure 2 shows the performance of the algorithm on the Standard Map at $k = 0.95$. Only 200 Poincaré points per surface were used in the algorithm, whereas 2000 points were used to generate the plot, to give the reader complete topological information. It is found that the algorithm generally classifies the surfaces correctly. The stochastic thickness parameter was 0.06 in these cases.

The second test case is characterization of actual stellarator magnetic fields for the CNT for the 64-deg tilt

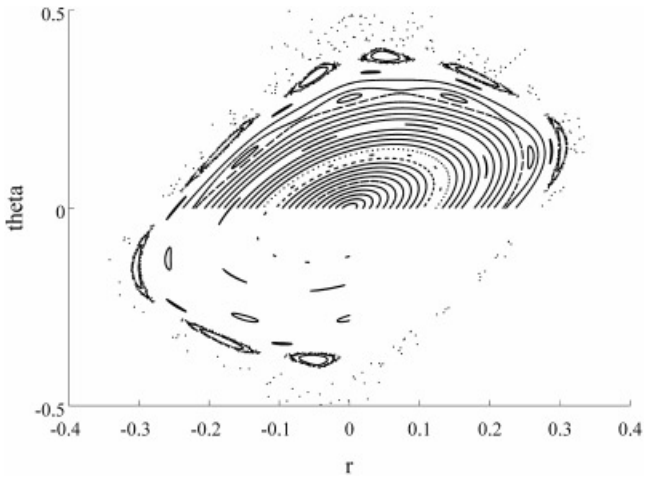

Fig. 2. The standard map for $k = 0.95$. The upper portion shows all the generated surfaces. The lower left shows stochastic regions and magnetic islands, whereas the lower right only shows the stochastic regions. For this case, 2000 Poincaré points per surface were used in generating the image, but only the first 200 were used in the surface characterization algorithm.

angle configuration, i.e., the configuration presently used in the experiment. Various perturbations to the magnetic coils are used to introduce islands and stochastic regions. By tuning the parameter g and the stochastic thickness parameter, one can obtain excellent results for both configurations; $g = 80$ works well for the CNT as well as for the Standard Map. Typically, only 200 Poincaré points per surface are needed to properly characterize the surfaces. The stochastic thickness parameter was 3 cm in these cases. Figure 3 shows an example of a perturbed equilibrium for the CNT (a 1-cm vertical shift of an interlocked coil) and its Poincaré plot, with surfaces properly classified.

The algorithm described above automatically establishes the thickness of any stochastic region and therefore can be used to adequately take into account the confinement degradation due to such regions. An additional algorithm has been added that analyzes the detected island chains. Each island in the island chain is clearly identified as a cluster of points with similar θ values, and the islands are separated by the gaps that were used to detect the island chain in the first place. Each cluster of points then identifies an island that is then analyzed in a relatively straightforward way to determine its total area and minor and major axes. Generally, one takes the minor axis to be the radial extent of the island (the island width).

The algorithm described above only works well if each magnetic field line is followed for several hundred transits, and it generally becomes more robust and accurate as the number of transits is increased. This is of course expected since even a human cannot tell whether a particular surface is broken into island chains unless substantially more points are presented than the number of islands in the island chain.

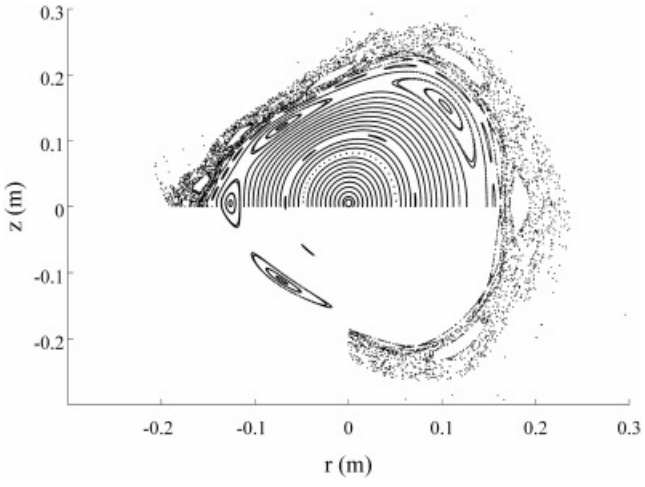

Fig. 3. A perturbed equilibrium of the CNT. The top half shows all the surfaces that were investigated. In the lower left, only islands are plotted, whereas only stochastic regions are plotted in the lower right. The algorithm correctly characterizes all the plotted surfaces.

The parameter g may need to be chosen differently for different classes of configurations in order to achieve optimum performance. However, the same value of g gives good performance on a variety of Poincaré plots produced with small differences in coil locations and coil currents. Therefore, the algorithm appears to be sufficiently robust that it can be useful in an actual stellarator optimization loop. In the case of the CNT, the choice of coil tilt angles and coil currents could in principle have been performed fully automated using this algorithm. However, the algorithm was developed after the main design choices were made based on a semimanual optimization that required human inspection of hundreds of Poincaré plots.

III. VACUUM SYSTEM

In the CNT, simple modeling performed prior to construction indicated that a vacuum level of 3×10^{-10} Torr or lower would ensure that neutrals and ions would be truly negligible for expected pure electron plasma parameters.[12] Although this level of vacuum is achieved in many experiments today, it is by no means a trivial matter in the CNT, which has a sizable volume (~ 6 m^3) and surface area (~ 10 m^2). Here, we describe the CNT vacuum system and its initial performance. The CNT vacuum chamber was built out of Type 316L stainless steel with all internal surfaces electropolished. All seals on the vacuum chamber were hard copper seals, and each internal coil had its own complete Type 316L stainless steel vacuum jacket, as described later in this article. There are several vacuum gate valves on the CNT. The valves are of the metal bonnet, viton seal type, typically bakeable to 150°C, rated to 1×10^{-10} Torr. The chamber and its internal components were designed to withstand a bake temperature of 200°C. The CNT pumping system consists of a roughing pump, a 60 ℓ/s turbopump, a UHV-compatible cryopump (Cryo-Torr 8 UHV-compatible version from Helix Technology, 4000 ℓ/s for water vapor, 2500 ℓ/s for molecular hydrogen), and a nonevaporable getter pump (SAES Getters Capacitorr B 1300, 1300 ℓ/s pumping speed for hydrogen). The roughing pump and turbopump are used to bring the chamber from atmospheric pressure to the 10^{-5} Torr range and are subsequently valved off as the cryopump is activated and brings the pressure further down. The cryopump is used from the 10^{-5} Torr range down to base pressure, and the getter pump is activated in the 10^{-8} Torr range. The main pumping in the UHV range is performed by the cryopump, which pumps all gases. The principal function of the getter pump, which pumps nearly all chemically active gases but no noble gases, is to lower the ultimate

pressure achieved by the system by providing efficient pumping of hydrogen in the 10^{-10} Torr range, where the hydrogen pumping capability of the cryopump is expected to be diminished because of the finite vapor pressure of hydrogen at 10 to 12 K, the temperature of the cold head on the cryopump. The getter and cryopump both have excellent pumping conductance to the vacuum chamber.

The empty CNT chamber was pumped down to 2.3×10^{-10} Torr following several vacuum bakeouts that successively lowered the base pressure. The maximum temperature on the vacuum chamber during bakeout was 200°C, but some parts of the chamber only reached ~140°C. The vacuum in the CNT is diagnosed using a 300-amu residual gas analyzer. At the 2.3×10^{-10} Torr base pressure, the primary vacuum constituent was hydrogen. In subsequent operation with the internal coils and various diagnostics and probes installed, pressures have been ranging from 2×10^{-8} Torr (without a bakeout) for field line mapping studies down to 1×10^{-9} Torr (after a 150°C bakeout) for pure electron plasma studies.

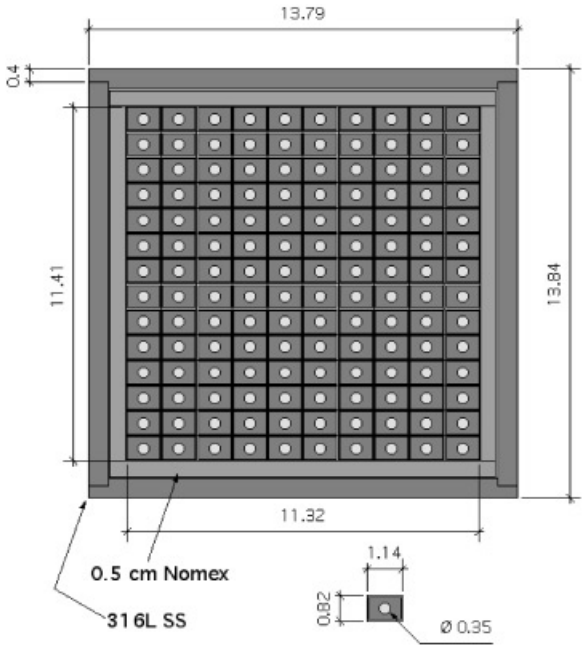

Fig. 4. A cross-sectional design view of one of the interlocked coils, showing the winding pack, Nomex insulation, and stainless steel vacuum case as well as the dimensions of the cross section of the rectangular copper conductor and its circular cooling channel. Units are in centimeters.

IV. DESIGN AND CONSTRUCTION OF IN-VESSEL INTERLOCKED COILS

The interlocked coils were wound interlocked, each consisting of 140 turns of rectangular copper conductor with a circular 4-mm-diam hole. The coils were wound as five double pancakes each with 2×14 turns. This allowed for relatively easy winding and for water cooling to occur in five parallel paths for each coil, greatly increasing the flow rate. The first coil was completed before the second one was wound, interlocked with the first one. The winding of the second coil required that a special winding table be assembled around the first coil, but other than that it was not a significant complication. The leads and turn transitions were placed at the top of the top coil and the bottom of the bottom coil to keep the associated magnetic field errors as far from the plasma as possible. The coil cross section is shown in Fig. 4.

In order to meet the stringent CNT vacuum specifications, the interlocked coils were encased in vacuum-tight Type 316L stainless steel cases. These cases were designed as inside-out vacuum chambers. Following standard UHV practice, the vacuum-tight welds were made from the vacuum side, that is, the outside of the coil cases, to avoid trapped volumes. The coil cases were electropolished prior to welding to reduce surface contaminants and effective surface area, and a layer of Nomex insulation was placed between the winding pack and the stainless steel cases to provide a thermal barrier. The primary purpose of this barrier was to allow a significant temperature differential between the vacuum cases and the actual winding pack so that the vacuum cases could be vacuum baked to 200°C without having the copper coils themselves exceed 90°C, by differential water cooling. The two interlocked coils are installed vertically in the vacuum chamber, with the ten leads from the top coil going through the top dome of the vacuum chamber and the ten leads from the bottom coil going through the bottom dome. The leads exit the main vacuum chamber through a custom knife-edged set of flanges. Three-dimensional (3-D) views of this arrangement are shown in Fig. 5. The design drawings of the custom flanges for the feedthrough are shown in Fig. 6. The dimensions and locations of the knife edges were chosen such that standard UHV copper gaskets and bolts can be used. The smaller custom flange is welded to the flexible bellows that brings the electrical leads out of the coil. It connects to the bottom of the larger custom flange, which also connects to a standard 25.4-cm-outer-diameter (o.d.) UHV flange on the vacuum chamber. Altogether, this provides the UHV seals necessary to isolate the atmospheric pressure on the outside of the vacuum chamber and the inside of the coil cases to the vacuum inside the vacuum chamber outside the coil cases. Additionally, a 20.3-cm-o.d. UHV flange was machined on the top of the 25.4-cm flange to allow for pumping on the inside of each coil case. This coupling was used when each interlocked coil was helium-leak checked by pulling a vacuum on the inside of the completed vacuum case prior to vacuum

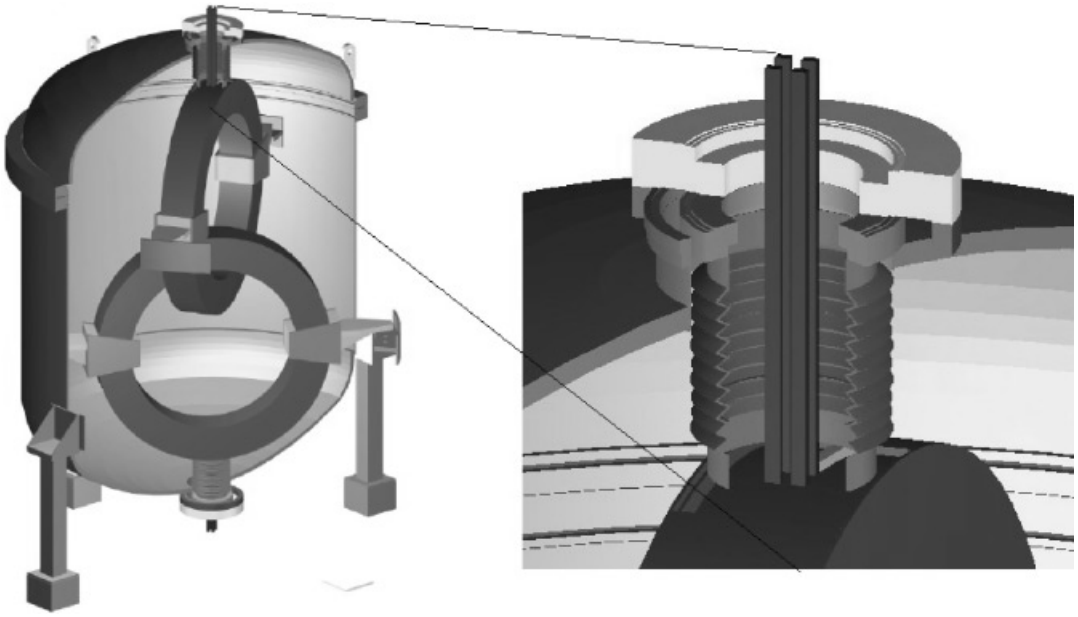

Fig. 5. A 3-D rendering of the interlocked coils and their integration with the main vacuum chamber. On the left, a cutaway view of the vacuum chamber, the interlocked coils, and the bellows and flanges used to bring the coil leads out. On the right, a zoom-in on the top flange arrangement, showing four out of the ten coil leads, the formed bellows, the custom 17.15-cm flange welded to the formed bellows, a rotatable 25.4-cm-o.d. flange on the vacuum chamber, and the custom 25.4-cm flange used to couple the other pieces together.

pressure impregnation. Helium spraying and helium bagging were then applied to the outside of each coil in succession.

V. STEADY-STATE OPERATION

Simple theoretical estimates of confinement times for pure electron plasmas on magnetic surfaces indicate that confinement can be extremely long, up to hours, and that this confinement should scale independently of the magnetic field strength, as long as the Debye length is small and the plasma is in equilibrium. For such long confinement times to be confirmed experimentally, one would need to be able to operate the CNT at a significant magnetic field strength essentially in steady state. Although the magnetic field strength does not enter into the theoretically predicted confinement scaling, it plays a critical role in ensuring that an equilibrium exists for a finite-density pure electron plasma. The ultimate density limit of any magnetically confined pure electron plasma is given by the Brillouin density, $n_B = \varepsilon_0 B^2/2m_e$, although for a stellarator, the equilibrium may break down at a far lower density, $n/n_B \approx 10^{-2}$ to 10^{-3} (Ref. 13).

The main experimental question for steady-state operation was to establish the maximum magnetic field strength achievable in steady state without causing the interlocked coil temperature to be unacceptably high. Steady-state operation of the PF coils is trivial by comparison because of their much lower current densities. Using water forced to flow through the circular cooling channel of the copper conductor, the CNT has been operated in steady state (several hours) at $B = 0.06$ T, with the interlocked coil outlet water temperature remaining below 50°C for an inlet temperature of ~12°C. At $B = 0.06$ T, $n_B = 1.75 \times 10^{16}$ m^{-3}, so for typical densities in the CNT, which are on the order of 10^{12} m^{-3} but may be as high as 10^{13} m^{-3} in future operation, the magnetic field is sufficiently high that an equilibrium is predicted to exist, as has recently been confirmed experimentally.

VI. MAGNETIC SURFACE MAPPINGS AND VISUALIZATIONS

The magnetic flux surface measurements in the CNT were carried out at the 64-deg tilt angle configuration for a variety of magnetic field strengths using the standard electron beam—fluorescent rod technique.[14] These results are reported in detail in Ref. 15 but are briefly summarized here. We also report on our techniques for 3-D visualizations of magnetic surfaces. The magnetic field line mapping measurements confirmed the existence of an ultralow aspect ratio ($A < 1.9$) set of nested magnetic surfaces in the CNT device, as predicted by numerical calculations. The main result is shown in Fig. 7.

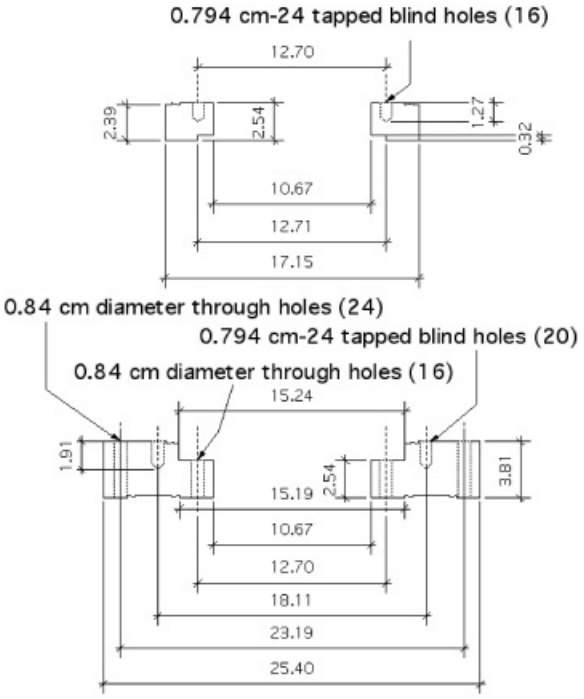

Fig. 6. The two custom knife-edged flanges for the interlocked coil feedthroughs. On the top, the 17.15-cm flange welded to the interlocked coil bellows. On the bottom, a 25.4-cm flange that connects to the 17.15-cm flange, using a standard copper gasket ordinarily used for 20.3-cm-o.d. flanges, and that also connects to a 25.4-cm-o.d. flange on the vacuum chamber using a standard copper gasket for use with 25.4-cm-o.d. gaskets. Units are in centimeters.

Although it is almost always necessary to confirm the magnetic surface topology in a stellarator, it was especially important in the CNT because it was built with rather loose tolerances (on the order of 10^{-2}) based on numerical simulations showing resilience against magnetic field errors arising from coil misalignments and manufacturing errors.

Experiments were also conducted to visualize the full 3-D shape of magnetic surfaces using an electron beam and neutral gas. The electron beam excites and ionizes the neutral gas, which emits visible light, allowing one to clearly see the electron beam as it travels along field lines. This allows a visualization of the whole magnetic surface on which the electron beam is injected. While field line mapping was performed at pressures in the 10^{-8} Torr range to avoid diffusion of the electron beam due to collisions with the background gas, the 3-D visualizations were carried out at much higher pressures in order to increase collisions with the residual gas to the level where the electron beam trace was clearly visible. Different background neutral gases (air, argon, and helium) were used, and the gas pressure and electron beam energy were also varied in the experiments. The optimum fill pressure is a trade-off between enhancing the visibility of the electron beam, yet keeping the diffusion low and the electron beam path length long, so it can traverse and visualize the entire magnetic surface. The best visualizations of glowing magnetic surfaces were obtained with a backfill of air at a pressure of 2 to 5 $\times$ 10^{-5} Torr using a 200-eV electron beam. Figure 8 shows an example of a glowing magnetic surface as could be seen with the naked eye through a quartz window on the chamber. Other relevant information, such as finding and visualizing the magnetic axis, can be obtained using this technique (as shown in Fig. 9). The technique will be used in the future to align probes so that they intersect the magnetic axis or a particular magnetic surface at some desired toroidal location. It may also be possible to use this technique to verify the rotational transform and the overall 3-D shape of the magnetic surfaces rather than just measuring one or two two-dimensional cross sections using the standard field line mapping technique.

VII. FIRST PURE ELECTRON PLASMAS

With the existence of nested high-quality magnetic surfaces confirmed, experiments to create pure electron

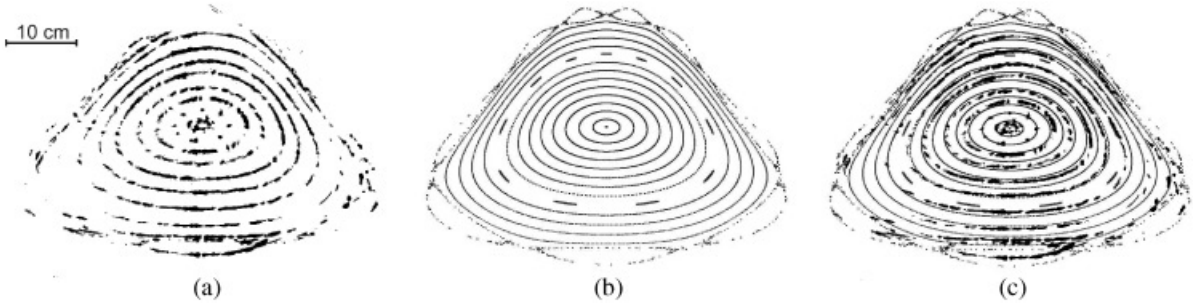

Fig. 7. (a) Nested magnetic surfaces mapped out using a 100-eV electron beam and ZnO-coated rods. (b) Numerically calculated magnetic surfaces for the 64-deg angle configuration. (c) The composite image overlaid on the numerical surfaces.

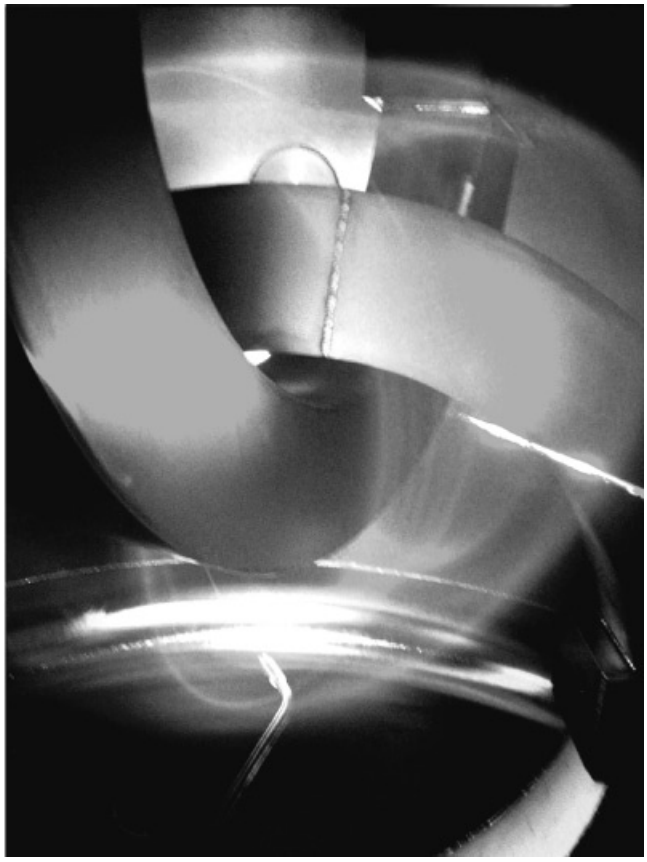

Fig. 8. Example of a glowing magnetic surface.

Fig. 9. A 3-D view of the magnetic axis.

plasmas have started. Electrons have been injected from several different multifilament electron emitters. The first emitter consisted of four thoriated tungsten filaments mounted on a hollow ceramic rod spaced ~8 cm apart to contact different magnetic surfaces. The filaments were operated independently in several ways. Heated, negatively biased filaments acted as sources of electrons, filling up the magnetic surfaces they were inserted on, through rapid parallel transport, and eventually filling the entire volume through cross-surface transport. Unbiased, heated filaments terminated to ground through 1-GΩ resistors were used as emitting floating probes. On this first emitter rod were metallic bands used to connect the tungsten and copper wires. These metallic bands were directly facing the plasma, and consequently, they would short-circuit the radial electric field. Acknowledging this problem, a second probe was constructed consisting of eight platinum tips, and four emitting tungsten filaments (from standard 12-V halogen light bulbs), mounted on a ceramic rod similar to the one used for the first probe. The amount of conductor directly exposed to the plasma was minimal in this case, except for the 12 small probe tips. An increase in confinement time of a factor of ~2 was observed when using the second emitter, presumably because of the reduced amount of exposed conductor material.

The first experiments in the CNT focused on confirming that the plasma volume could be filled with a significant number of electrons. The data were taken over several seconds, so a steady state had established between the electron emission and the electron losses. Configuring three of the four filaments as floating emitting probes, the floating potential was measured at three different radial locations. The floating potential of an emitting probe is approximately $\phi_f = \phi_p - \alpha T_e/e$, unless the electron density is very low or the impedance to ground is not sufficiently high, in which case ϕ_f will be closer to zero (Ref. 16). Here, $\alpha \leq 1$, at least in a neutral plasma.[17] An example of a potential profile measurement is shown in Fig. 10.

The fact that the floating potentials measured were on the order of the filament bias potential indicates that the volume was indeed filled with electrons. For the example shown in Fig. 10, the roughly −300-V potential on filaments terminated to ground through 1-GΩ resistors implies that each is collecting ~300 nA of negative current. This would not be possible if there were little or no space charge on the magnetic surfaces

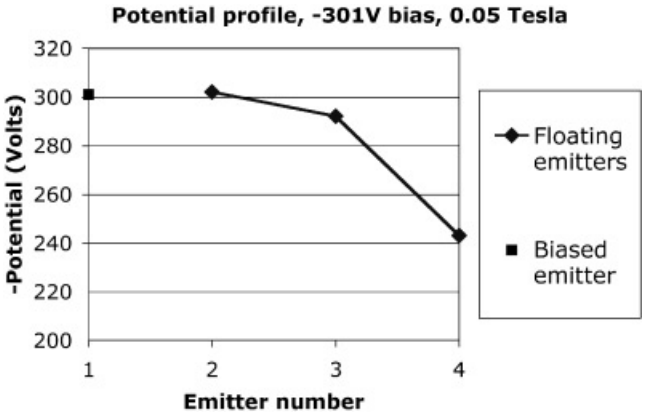

Fig. 10. A typical potential profile for a plasma created with a −300-V bias on the innermost emitter, which was placed near the magnetic axis. These emitters were spaced ~8 cm apart, with the fourth emitter inside but near the last closed flux surface.

on which the floating emitting filaments were placed. When the biased emitter was either cold or unbiased, the potentials on the floating emitters were essentially zero, as expected.

Extrapolation of these measurements was used to estimate the electrostatic potential difference between the magnetic axis and the last closed flux surface, assuming that the temperature is low enough that the floating potential profile approximates the plasma potential profile well. This difference, $\Delta\phi$, can then be used to estimate the total electron inventory. A simple circular cylindrical estimate, assuming constant electron density and a cylinder length of $2\pi R$ yields a total electron inventory $N = 8\pi 2\varepsilon_0 R\Delta\phi/e$.

For a particular experiment with a neutral pressure of 5×10^{-9} Torr, $B = 0.05$ T, a bias of -150 V was applied to the innermost emitting filament, yielding roughly $\Delta\phi \approx 80$ V and $N \approx 10^{11}$ electrons, according to this estimate. The remaining 70-V potential difference is thought to occur in the vacuum region between the last closed flux surface and the grounded vacuum chamber and coils.

For this particular experiment, the steady-state emission current from the biased emitter (the source of electrons) was 1.5 μA, that is, 10^{13} e/s, and hence, the confinement time was ~10 ms. In the complete absence of a magnetic field, the filament emission current was in the milliampere range. Further experiments and more detailed measurements, which will be reported in a future article, have confirmed that the estimated electron inventory and confinement time for the initial experiments reported here were correct to within a factor of 2 and that the Debye criterion ($a \gg \lambda_D$) is satisfied, i.e., the electron clouds created are truly electron plasmas.

VIII. CONCLUSIONS

Construction of the CNT was successfully completed in November 2004. The design goals of the CNT have largely been met. Neutral pressures in the 10^{-10} to 10^{-9} Torr range have been achieved, which is adequate for nonneutral plasma research. The design specification of $<3 \times 10^{-10}$ Torr has been met for the empty vacuum chamber, whereas more work needs to be done to achieve this with the internal coils, probes, and emitters present inside the vacuum chamber. High-quality ultralow aspect ratio magnetic surfaces have been measured experimentally, confirming the numerical predictions that these could be achieved with simple coils and construction tolerances on the order 0.5 to 1%, which is loose by stellarator standards. Pure electron plasmas have been created by electron emission from heated bare filaments inserted into the magnetic surfaces. Thus, the experiment has successfully started to explore the physics of nonneutral plasmas confined on magnetic surfaces.

ACKNOWLEDGMENTS

This work was supported by the U.S. Department of Energy under grant DE-FG02-02ER54690, by the National Science Foundation (NSF)-DOE Partnership in Basic Plasma Science under grant NSF-PHY-04-49813, and by the Princeton Plasma Physics Lab Off-site University Support Program.

REFERENCES

1. T. SUNN PEDERSEN and A. H. BOOZER, *Phys. Rev. Lett.*, **88**, 205002 (2002).

2. T. SUNN PEDERSEN, A. H. BOOZER, W. DORLAND, J. P. KREMER, and R. SCHMITT, *J. Physics B*, **36**, 1029 (2003).

3. T. SUNN PEDERSEN, A. H. BOOZER, J. P. KREMER, and R. LEFRANCOIS, *Phys. Plasmas*, **11**, 2377 (2004).

4. T. SUNN PEDERSEN, A. H. BOOZER, J. P. KREMER, R. LEFRANCOIS, F. DAHLGREN, N. POMPHREY, W. REIERSEN, and W. DORLAND, "The Columbia Nonneutral Torus: A New Experiment to Confine Nonneutral and Positron-Electron Plasmas in a Stellarator," *Fusion Sci. Technol.*, **46**, 200 (2004).

5. C. GOURDON, D. MARTY, E. A. MASCHKE, and J. P. DUMONT, *Proc. 3rd Int. Conf. Plasma Physics Controlled Nuclear Fusion Research*, Vienna, Austria, p. 847, International Atomic Energy Agency (1969).

6. T. ESTRADA et al., *Plasma Phys. Control. Fusion*, **46**, 277 (2004).

7. K. TANAKA et al., *Plasma Phys. Control. Fusion*, **44**, A231 (2002).

8. S. R. HUDSON and R. L. DEWAR, *Phys. Lett. A*, **226**, 85 (1997).

9. K. MAN-KAM YIP, "KAM: A System for Intelligently Guiding Numerical Experimentation by Computer," MIT Press, Cambridge, Massachusetts (1991).

10. A. BAGHERJEIR and C. KAMATHAN "Graph-Based Methods for Orbit Classification," Internal Report UCRL-CONF-215802, Lawrence Livermore National Laboratory (2005).

11. B. CHIRIKOV, *Phys. Rep.*, **52**, 265 (1979).

12. T. SUNN PEDERSEN, A. H. BOOZER, and J. P. KREMER, *Proc. Non-Neutral Plasma Workshop*, Santa Fe, New Mexico, p. 302, American Institute of Physics (2003).

13. A. H. BOOZER, *Phys. Plasmas*, **12**, 104502 (2005).

14. R. JAENICKE, E. ASCASIBAR, P. GRIGULL, I. LAKICEVIC, A. WELLER, M. ZIPPE, H. HAILER, and K. SCHWORER, *Nucl. Fusion*, **33**, 687 (1993).

15. T. SUNN PEDERSEN, J. P. KREMER, R. LEFRANCOIS, Q. MARKSTEINER, X. SARASOLA, and N. AHMAD, *Phys. Plasmas*, **13**, 012502 (2006).

16. H. HIMURA, M. FUKAO, H. WAKABAYASHI, and Z. YOSHIDA, *Rev. Sci. Instrum.*, **74**, 4658 (2003).

17. M. Y. YE and S. TAKAMURA, *Phys. Plasmas*, **7**, 3457 (2000).